ACS APPLIED MATERIALS & INTERFACES

www.acsami.org

Research Article

# Modeling LiF and FLiBe Molten Salts with Robust Neural Network Interatomic Potential

Stephen T. Lam,* Qing-Jie Li, Ronald Ballinger, Charles Forsberg, and Ju Li

Cite This: *ACS Appl. Mater. Interfaces* 2021, 13, 24582–24592

Read Online

ACCESS | Metrics & More | Article Recommendations

**ABSTRACT:** Lithium-based molten salts have attracted significant attention due to their applications in energy storage, advanced fission reactors, and fusion devices. Lithium fluorides and particularly 66.6%LiF−33.3%$BeF_2$ (Flibe) are of considerable interest in nuclear systems, as they show an excellent combination of favorable heat transfer, neutron moderation, and transmutation characteristics. For nuclear salts, the range of possible local structures, compositions, and thermodynamic conditions presents significant challenges in atomistic modeling. In this work, we demonstrate that atom-centered neural network interatomic potentials (NNIPs) provide a fast method for performing molecular dynamics of molten salts that is as accurate as ab initio molecular dynamics. For LiF, these potentials are able to accurately reproduce ab initio interactions of dimers, crystalline solids under deformation, crystalline LiF near the melting point, and liquid LiF at high temperatures. For Flibe, NNIPs accurately predict the structures and dynamics at normal operating conditions, high-temperature−pressure conditions, and in the crystalline solid phase. Furthermore, we show that NNIP-based molecular dynamics of molten salts are scalable to reach long time scales (e.g., nanosecond) and large system sizes (e.g., $10^5$ atoms) while maintaining ab initio density functional theory accuracy and providing more than 3 orders of magnitude of computational speedup for calculating structure and transport properties.

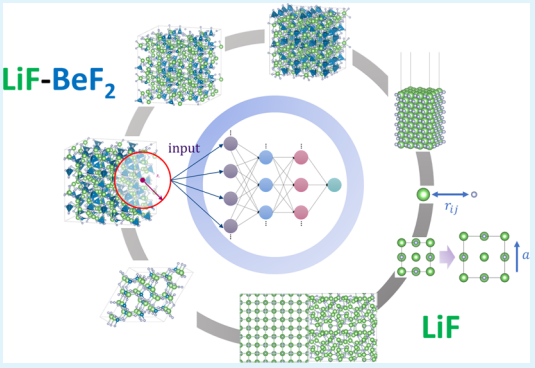


**KEYWORDS:** *nuclear energy, molten salt, lithium fluoride, atomistic simulation, neural networks*

## 1. INTRODUCTION

Molten salts are important high-temperature liquids for many industrial applications such as waste oxidation, catalytic coal gasification, concentrated solar power, and advanced nuclear reactors.[1−5] Generally, the modeling of ionic liquids poses interesting challenges considering the complexities in modeling various atomic structures, multiple phases (solid, liquid, vapor, and glass), and transformations that can dramatically change the salt's properties.[6] For advanced fission and compact fusion reactors, lithium-based fluoride salts are the material of choice owing to their high actinide solubility and desirable heat transfer characteristics.[7] Specifically, LiF−$BeF_2$ mixtures have been identified as important prototype salts in reactor systems in the thermal neutron spectrum. This is because (1) LiF−$BeF_2$ salts show reasonably good neutron moderation and low neutron absorption and (2) LiF is a common constituent used to depress a mixture's melting point, thus reducing the chance of salt freezing. Furthermore, Li is desirable in fusion systems due to its ability to generate nuclear fuel as tritium.

In the past two decades, physics-based interatomic potentials have been developed for molten salts using ab initio force-fitting methods. Such empirical potentials often require an explicit definition of the potential energy functional form and assumptions about the relevant interactions in a given salt mixture. For example, the polarizable ion model (PIM) is commonly used for molten salts, which includes charge−charge interaction, repulsion, dispersion, and polarization effects.[8,9] While such models have been highly successful for calculating thermophysical and thermodynamic properties of binary and even ternary mixtures,[9,10] they and other classical potentials are subject to limitations of accuracy and generality.[11] Such models are limited to specific systems for which parameters are developed and are generally expected to be less accurate as the system complexity increases.[8] For example, a recent study found that PIM potential could not systematically produce accurate melting points across different alkali chlorides, which was attributed to inaccuracies in simultaneously representing solid and liquid phases.[12] Moreover, most classical potentials are unable to capture charge transfer,

Received: January 13, 2021
Accepted: April 6, 2021
Published: May 21, 2021

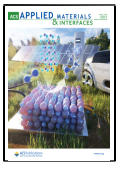







https://doi.org/10.1021/acsami.1c00604
*ACS Appl. Mater. Interfaces* 2021, 13, 24582−24592

speciation, and chemical bonding. This is particularly relevant in high-temperature molten salt systems, where operating conditions can vary greatly, and selecting from salt mixtures containing many possible interacting constituents are of interest. On the other hand, machine-learning-based methods such as artificial neural networks are considered universal function approximators, thus representing a new paradigm for modeling molten salt atomic systems. In this work, we trained two NNIPs using LiF and Flibe (66.6%LiF−33.3%$BeF_2$) as our model systems due to their relevance in technological application and their intrinsically interesting properties. The LiF system is included since it is relatively simpler and has a well-defined crystalline solid structure that can be studied to test and validate the NNIP method. In Flibe, the mixture of monovalent Li and divalent Be results in heterogeneous ion transport behavior, causes a number of chemical reactions with impurities, and forms extended structures like $BeF_2$ corner-sharing polyhedral chains.[13] Thus, the combination of these two salts provides good prototypes for testing NNIPs in molten salt applications.

## 2. METHODS

**2.1. Materials and Salt Systems.** To train a robust neural network capable of capturing a range of local atomic environments, a variety of different systems were included. For the LiF potential, the total ab initio data set includes 4200 images of atomic pairs (1400 F−F, 1400 Li−F, and 1400 Li−Li) at different separation distances, 1400 solid crystalline configurations at 0 K under ±20% deformation, 6000 solid configurations at 1050 K, 6000 crystalline LiF near the melting point at 1120 K, and 8000 liquid LiF configurations at 1200 K. All LiF configurations were sampled at experimental density.[14] For Flibe, all configurations were sampled at experimental density with ab initio molecular dynamics.[15] This consists of 8000 configurations at 973 K, 4000 configurations at 973 K under 15% compression, and 4000 configurations at a high temperature of 5000 K. All finite temperature configurations were subsampled from ab initio molecular dynamics trajectories, as described by the following section.

**2.2. Ab Initio Data Generation.** The accuracy of neural network models is fundamentally limited by the quality of ab initio data used to develop the NNIPs. Here, training and validation data were generated using density functional theory (DFT)[16] and Born−Oppenheimer ab initio molecular dynamics (AIMD).[17] AIMD sampling was performed in the canonical (*NVT*) ensemble using a time step of 2 fs and a Nosé-mass corresponding to a decay time of 80 fs. Configurations were uniformly sampled from AIMD trajectories every 10 fs to reduce correlation in the input data. Calculations were performed using the Vienna ab initio simulation package (VASP)[18] with the plane-wave basis set and periodic boundary conditions in all cell directions. For LiF, pair interactions were calculated based on dimer configurations in a cubic cell with a side length of 24 Å. For the crystalline solid at 0 K, an 8-atom unit cell is used with a 3 × 3 × 3 Γ-centered **k**-point grid. LiF AIMD simulations of solid and near-melting point crystalline systems were performed for 60 ps for systems containing 64 atoms, and liquid simulations were performed for 80 ps for a system containing 70 atoms. All AIMD systems used a 2 × 2 × 2 **k**-point sampling on a Γ-centered grid. In all cases, a plane-wave energy cutoff of 550 eV was used. For Flibe, all configurations contained 91 atoms (26 Li, 52 F, and 13 Be), and the AIMD sampling was based on a plane-wave energy cutoff of 600 eV and Γ point-only Brillouin zone sampling. Simulations at 973 K, under 15% compression, and at 5000 K were performed for 80, 40, and 40 ps, respectively. The **k**-point sampling density and plane-wave energy cutoff were chosen to ensure an energy convergence of <2 meV/atom between different calculations.[13] All calculations were performed using the Perdew−Burke−Ernzerhof (PBE) generalized gradient approximation (GGA) exchange−correlation functional and projector-augmented wave (PAW) potentials for the nucleus and core electrons (Li_sv, Be, and F). These simulation protocols were previously validated for a variety of fluoride salts to produce accurate predictions for a variety of chemical and physical properties.[13]

**2.3. Neural Network Interatomic Potentials.** Neural network potentials have seen success in accurately modeling potential energy surfaces for a wide range of materials and applications.[19,20] For high-dimensional systems, NNIPs are among the more advanced machine-learning methods and are largely based around the methodology of Behler−Parinello (BP), which uses an atom-centered approach to train neural networks taking local atomic features as input to provide scalability.[21] Here, the total energy is considered as the sum of energy contributions of individual atoms $i$ in the system $E_{tot} = \sum_{N_{at}} E_i(\mathbf{G}_i)$, where the local atomic environment is captured by a vector of input functions $\mathbf{G}_i$, which represent the atomic environment around a central atom $i$. Different methods and functions have been developed for generating $\mathbf{G}_i$, which prioritize usability, efficiency, and accuracy in various applications.[21−25] In this work, we adopt and describe functions from Smith et al.[26] and Lot et al.,[24] which are an improvement on the BP's original work.[21] In our recent studies, we found this method to be sufficiently robust and efficient for modeling and calculating properties for molten NaCl.[27]

The functions we used consist of two-body and three-body descriptors, which capture the radial and angular environments, respectively. For a central atom $i$, the radial descriptor is defined as the sum of Gaussian functions

$$G_i^{\mathrm{R}} = \sum_{j \neq i}^{N_p} e^{-\eta(R_{ij}-R_S)^2} f_c(R_{ij}) \tag{1}$$

where $\eta$ and $R_S$ represent the width and offset of the Gaussian, respectively, $R_{ij}$ is the distance between atoms $i$ and $j$, and the sum is taken over all ion pairs $N_p$ within a cutoff that is defined by function $f_c$

$$f_c(R_{ij}) = 0.5 \cos\left(\frac{\pi R_{ij}}{R_c}\right) + 0.5, \quad \text{for} \quad R_{ij} < R_c$$
$$f_c(R_{ij}) = 0, \quad \text{for} \quad R_{ij} < R_c \tag{2}$$

This cutoff function presents a smooth decay to zero at the limit of a defined $R_c$, which was chosen to be 7 Å. The smooth cutoff ensures that the function is continuously differentiable, enabling the reliable calculation of forces for molecular dynamics simulations. This cutoff radius value was found to be a sufficient approximation for property prediction. The angular descriptor is defined

$$G_i^{\mathrm{A}} = 2^{1-\zeta} \sum_{j,k \neq i}^{N_t} (1 + \cos(\theta_{ijk} - \theta_S))^{\zeta} e^{-\eta((R_{ij}+R_{ik})/2-R_S)^2} f_c(R_{ij}) f_c(R_{ik}) \tag{3}$$

where $\zeta$ is the width of the Gaussian function, $\theta_s$ is the cosine offset, and $\theta_{ijk}$ is the angle formed by atoms $i$, $j$, and $k$, and the sum is taken over all triplets within $R_c$. The angular and radial functions are calculated based on different sets of hyperparameters ($\zeta$, $\theta_S$, $R_S$), which are then concatenated into a neural network input vector $\mathbf{G}_i$. In this way, the resolution of the feature space can be arbitrarily increased by sampling the hyperparameters at increasingly fine intervals. The general method is discussed in more detail by Smith.[26] In this work, the hyperparameter sets were all combinations of $R_c$ = 7.0 Å, $\eta$ = 12.0, $\zeta$ = 50.0, $R_{S(\mathrm{radial})}$ = {0.5, 0.75, ...,7.75} Å, $R_{S(\mathrm{angular})}$ = {2, 2.5,...,5.5} Å, and $\theta_S = \left\{0, \frac{1}{6}\pi, \frac{1}{3}\pi, \frac{1}{2}\pi, \frac{2}{3}\pi, \frac{5}{6}\pi\right\}$. Thus, the size of $\mathbf{G}_i$ is 168 for LiF (I = Li, F) and 294 for Flibe (I = Li, Be, F), serving as input into a corresponding neural network based on the species of the central atom $i$.

Neural networks are trained using mini-batch gradient descent with the Adam optimization algorithm[28] using a decaying learning rate from 1 × $10^{-3}$ to 1 × $10^{-4}$. This was used to minimize the cost function $J$


https://doi.org/10.1021/acsami.1c00604
ACS Appl. Mater. Interfaces 2021, 13, 24582−24592

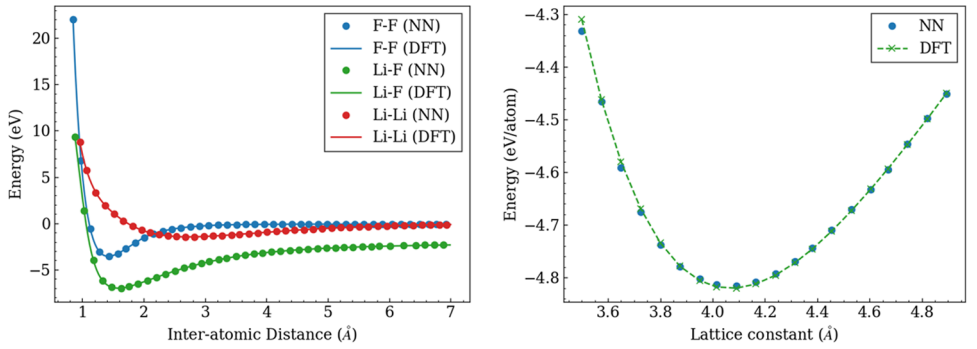


**Figure 1.** DFT versus NN predictions for (a) pair interactions for Li−F, Li−Li, and F−F and (b) equation of state for the bulk B1 phase LiF at 0 K.[30]

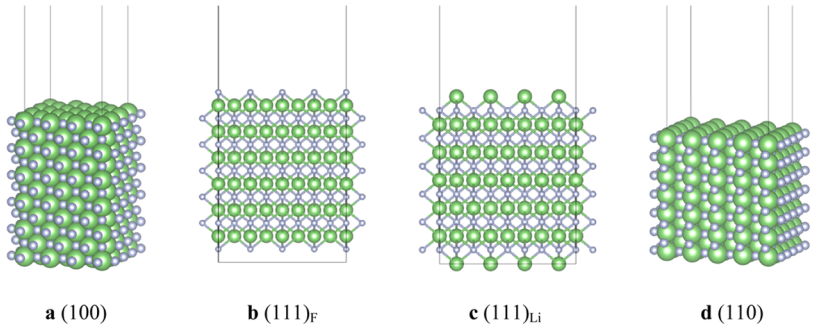


**Figure 2.** LiF surfaces with different surface terminations and 1:1 Li/F stoichiometry, (a) (110), (b) $(111)_F$ terminated with F, (c) $(111)_{Li}$ terminated with Li, and (d) (110).

$$J(\mathbf{W}) = \sum_{i\in\text{batch}} \left[ (E_i^{\text{DFT}} - E_i^{\text{NN}}(\mathbf{W}))^2 + \frac{c_f}{3N_i} \sum_{j=1}^{N_i} \sum_{k\in\{x,y,z\}} (F_{ij}^{\text{DFT},k} - F_{ij}^{\text{NN},k}(\mathbf{W}))^2 \right] + C_{\mathbf{W}} \|\mathbf{W}\|^2 \quad (4)$$

where $\mathbf{W}$ is the weight matrix that parameterizes the neural network, $E_i$ is the energy of an atomic configuration $i$ calculated by DFT or NN, $F_{ij}^k$ is the forces of atom $j$ in the configuration $i$ in the direction $k$, $c_f$ is a factor to weight the relative importance of obtaining accurate forces, and $c_W$ is the regularization constant. Here, a batch size of 100 configurations is used, $c_f$ = 0.2, and $c_W$ = 0.1 is used to prevent overfitting of the neural network. For LiF, all of the atomic neural networks consist of two fully connected hidden layers with 64 nodes each. A similar architecture is also used for Flibe, except with 32 nodes in each layer. The Gaussian activation function was used in hidden layer nodes, and linear activation was used in the output node. In each salt system, 80% of the total data is used for training and tuning and the remaining 20% is withheld and used as the test set. The training is conducted using the PANNA package.[24] Molecular dynamics simulations with the neural network potentials are then performed in LAMMPS.[29]

## 3. RESULTS

**3.1. LiF Binary Salt Potential.** *3.1.1. Pair Interactions, Bulk EOS, and Surfaces.* A variety of atomic configurations are used to train and test the neural networks, as described in Section 2.1. In addition, various high-index surfaces that were not seen by the network were also calculated and compared to the DFT values to assess the ability of the network to extrapolate. First, dimer interactions predicted by the neural network are shown in Figure 1a for Li−F, F−F, and Li−Li. In all cases, the neural network predictions and DFT calculations agree very well. The flattening of the tails on the potential energy curve is accurately predicted by the neural network, which means that the medium-range contributions to force are accurately represented. The high-energy repulsion at a short interatomic distance is also accurately reproduced. At short interatomic distances, accuracy is limited by the DFT data themselves due to the use of pseudopotentials to model the nucleus and core electrons. These high-energy interactions are important when simulating liquids at high temperatures where a large number of configurations are sampled, and high-energy collisions can occur. Further, accurate calculation of these energies reduces energy drift due to time integration for molecular dynamics simulations in the microcanonical ensemble (*NVE*). In all species pairs, the equilibrium distance (minimum energy) is also reproduced. Across the range of atomic distances, this accuracy is found sufficient for molecular dynamics.

Using the same neural network, the equation of state for bulk solid phase B1 is also fit, as shown in Figure 1b. Energy data was collected for different cell volumes, and the equilibrium lattice constant is calculated as 4.07 Å at the minimum energy, which is consistent with previous calculations within ± 0.01 Å.[31] The neural network prediction is in good agreement with DFT calculations with a mean average error (MAE) of <8 meV/atom. At large compression, the error is higher due to poorer sampling in that region. This accuracy can be improved by adding more high-energy configurations into the training data. For the calculations here, the accuracy is


https://doi.org/10.1021/acsami.1c00604
ACS Appl. Mater. Interfaces 2021, 13, 24582−24592

sufficient since most simulations are performed either at or near equilibrium density. Moreover, the energy $E(\mathbf{r})$ for pair and EOS interactions is smooth and continuous, which allows for accurate calculation of forces and stresses.

Surface energy calculations were also performed with neural networks and compared to DFT results under different local environments (coordination, species density, symmetry). The slabs were constructed with 11−13 layers. The DFT calculations were performed using a 3 × 3 × 1 **k**-point mesh. Graphical representations of some of the calculated surfaces are shown in Figure 2. The surface energy $\gamma$ is calculated as follows

$$\gamma = \frac{E_{slab} - NE_{bulk}}{2A} \quad (5)$$

where $E_{slab}$ is the calculated energy of the slab, $N$ is the number of formula units of LiF in the slab, $E_{bulk}$ is the energy of a bulk crystal per unit, and $A$ is the area of the slab's surface. In each cell, a 20 Å thick vacuum is added on top of the slabs to limit interactions with periodic images. In this work, we are interested in the neural network prediction of DFT calculations in low coordination environments rather than providing detailed study of LiF surfaces, which has been the work of previous studies.[32] Thus, optimization and testing of various minimum energy structures were not performed. We therefore note that the surface energies calculated here should not be taken as precise determination of values that should be compared to experimental values. As such, calculations were performed with only ionic relaxation of the two outer layers. For the (111) surfaces, 1/2 of the atoms were removed from the top and bottom layers to preserve a 1:1 Li/F stoichiometry. Here, there are two possible surfaces: one with Li-termination $(111)_{Li}$ and one with F-termination $(111)_F$ as shown in Figure 2b,c. We note that this differs from other proposed (111) surfaces, such as the octopolar reconstructed surface where 1/4 of the atoms in the outermost layer and 3/4 of the atoms on the subsequent layer are removed.[32]

The surface energies calculated from DFT are compared to the neural network in Table 1 for the (100), (110), $(111)_{Li}$, and $(111)_F$ surfaces. The DFT-calculated surface energies ranged from 34.6 to 67.2 meV/Å$^2$, representing a broad range of values. We note that the surface energy for (100) is in excellent agreement with previous calculations despite various approximations made in the system setup and structural optimization.[33] In all cases, the predicted surface energies are relatively close to the DFT energies, with the greatest error in $(111)_{Li}$, where the neural network underpredicts the surface energy by 4.1 meV/Å$^2$. Considering that local chemical coordinations for these surfaces are significantly different (in species and number) compared to bulk crystal or liquid configurations, which comprised a vast majority of training data, these calculations suggest that the neural network potential has good transferability and performs well over a range of environments.

**Table 1. Calculated Surface Energies from DFT versus Neural Networks**

| surface | DFT (meV/Å$^2$) | NN (meV/Å$^2$) |
|---|---|---|
| (100) | 34.6 | 36.8 |
| (110) | 47.0 | 49.9 |
| $(111)_{Li}$ | 63.5 | 59.4 |
| $(111)_F$ | 67.2 | 64.0 |

*3.1.2. Solid-to-Liquid Phases of LiF.* The neural network interatomic potential was used to calculate energies and forces for atomic configurations, including solid crystalline LiF, crystalline LiF near the melting point, and liquid LiF. A single NNIP that accurately simulates all of these configurations is desirable since it would allow for phase transitions over the range of potential operating conditions. Specifically, the prediction of salt properties near the phase boundaries is useful in understanding melting and freezing transitions that are critical to the safety of molten salt reactors.[7] Snapshots of the atomic configurations are shown in Figure 3. As shown, crystalline solids near $T_m$ contain large localized atomic displacements while maintaining a partially ordered structure, while liquid configurations are highly disordered. The disorder of the liquid state is confirmed by the calculation of radial distribution functions (RDFs) in the previous work.[13]

The test errors of NNIP vs DFT results for all three phases are shown in Figure 4. Both the training and test errors in energy and force predictions are shown in Table 2. Figure 4a shows the ab initio vs neural network energy calculation for the test data, where data is colored based on the configuration type: solid, solid near $T_m$, and liquid salt. As shown, energy prediction is as accurate as DFT across the range of configurations and coordination environments. The error histograms fit to Gaussians are shown in Figure 4b. As temperature increases, the error distributions widen with standard deviations of 0.75, 1.0, and 1.8 meV/atom for solid, solid near $T_m$, and liquid salt phases, respectively. This is caused by the wider distribution of energy values at higher temperatures creating a distribution in the configuration-space sampling, which drives the neural network prediction error. Finally, the ab initio forces are compared with neural network calculations in Figure 4c, which again shows good agreement with an MAE of 0.06 eV/Å.

Overall, the agreement between the neural network and DFT calculation is excellent with all energy test errors <2.3 meV/atom and force errors <0.08 eV/Å. This is near the precision of the DFT calculations used to generate the reference data, where **k**-point density and plane-wave energy cutoffs were converged up to a precision of 2 meV/atom. The energy span between the liquid and solid phase configurations is $E_{max} - E_{min} \sim 245$ meV. Thus, the relatively low error in the test set combined with the good force prediction suggests that the NNIP is well trained to interpolate between configurations in different phases and is robust across a range of coordination environments.

**3.2. LiF−$BeF_2$ Potential.** *3.2.1. Energy and Force Prediction.* For Flibe, a potential is trained by sampling Flibe configurations from both normal operating and extreme pressure and temperature conditions (973 K, 15% compression at 973, 5000 K fixed at the experimental density) shown in Figure 5c. The neural network and ab initio energies and forces are compared in Figure 5, while the training and test errors are shown in Table 3. For both energies and forces, the NNIP shows excellent agreement with the DFT data regardless of different atomic species or configurations. Specifically, the training MAEs in energies and forces are 1.75 meV/atom and 0.081 eV/Å, respectively. The test errors are slightly higher at an energy MAE of 2.10 meV/atom and a force MAE of 0.084 eV/Å. These energies are well within the so-called chemical accuracy, on the same order of errors inherent in DFT


https://doi.org/10.1021/acsami.1c00604
ACS Appl. Mater. Interfaces 2021, 13, 24582−24592

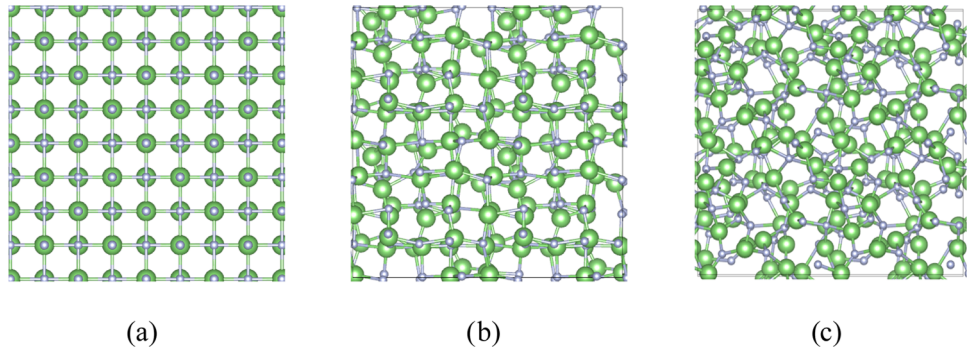


**Figure 3.** Graphical representation of LiF showing a 2 × 2 × 2 supercell for (a) solid crystalline bulk B1 phase at 1050 K, (b) crystalline solid near the melting point of 1120 K, and (c) molten LiF at 1200 K.

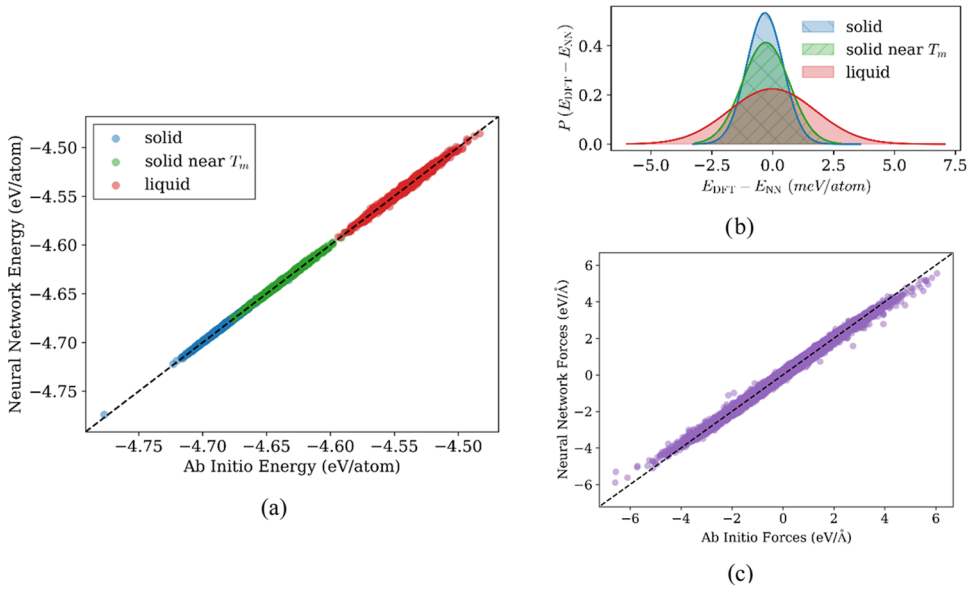


**Figure 4.** LiF neural network test errors. (a) Parity plot for solids, solids near $T_m$, and liquids calculated from neural networks and AIMD; (b) normalized probability density function of energy errors; and (c) force parity plot for all calculations.

**Table 2. Training and Testing Errors on Energy and Forces for Different Phases of LiF**

| | error (MAE) | solid | solid near $T_m$ | liquid |
|---|---|---|---|---|
| energy (meV/atom) [kJ/mol (LiF)] | train | 1.0 [0.19] | 1.0 [0.19] | 1.3 [0.25] |
| | test | 1.6 [0.31] | 2.3 [0.44] | 2.1 [0.41] |
| forces (eV/Å) | train | 0.04 | 0.04 | 0.04 |
| | test | 0.08 | 0.05 | 0.06 |

calculation due to **k**-point sampling, and approximations in the selection of a finite plane-wave basis set. The good agreement of forces in the test set indicates that the potential energy surface is not overfit since the gradients are accurately computed in the test set, which was not used to train the network. Moreover, the NNIP shows a good approximation in different structural environments, as shown in Figure 5c. The formation of $BeF_4$ tetrahedra can be seen at 973 K, which was also found in previous studies.[13,34] At 5000 K, tetrahedra start to dissociate as a result of high-energy collisions. In contrast, more $BeF_4$ tetrahedral and tetrahedral chains emerge when Flibe is compressed due to increased density and reduced ionic mobility.

To further test the versatility and transferability of the NNIP, we calculated the formation energy of purely crystalline Flibe,[35,36] which was not used in training. The Flibe crystal structure is shown in Figure 5c(4). The formation energy $E_f$ per atom is calculated

$$E_f \equiv E_{\text{Flibe}} - \frac{n_F}{N}E_F - \frac{n_{Li}}{N}E_{Li} - \frac{n_{Be}}{N}E_{Be} \quad (6)$$

where $E_{\text{Flibe}}$ is the energy per atom of the crystalline Flibe configuration, $E_F$, $E_{Li}$, and $E_{Be}$ are the per-atom energies of the ground-state structures of each species,[37−39] and $n_F$, $n_{Li}$, $n_{Be}$, and $N$ are the number of atoms of each element (24, 12, and 6) and total number of atoms in the computed Flibe cell, respectively. The DFT calculation is consistent with the methods described in Section 2.2. Here, we find that the formation energies from DFT and NN are generally in agreement at −3.356 eV/atom (−755.5 kJ/mol) and −3.333 eV/atom (−750.4 kJ/mol), respectively, which is close to chemical accuracy. Since the crystal structure was never seen


https://doi.org/10.1021/acsami.1c00604
ACS Appl. Mater. Interfaces 2021, 13, 24582−24592

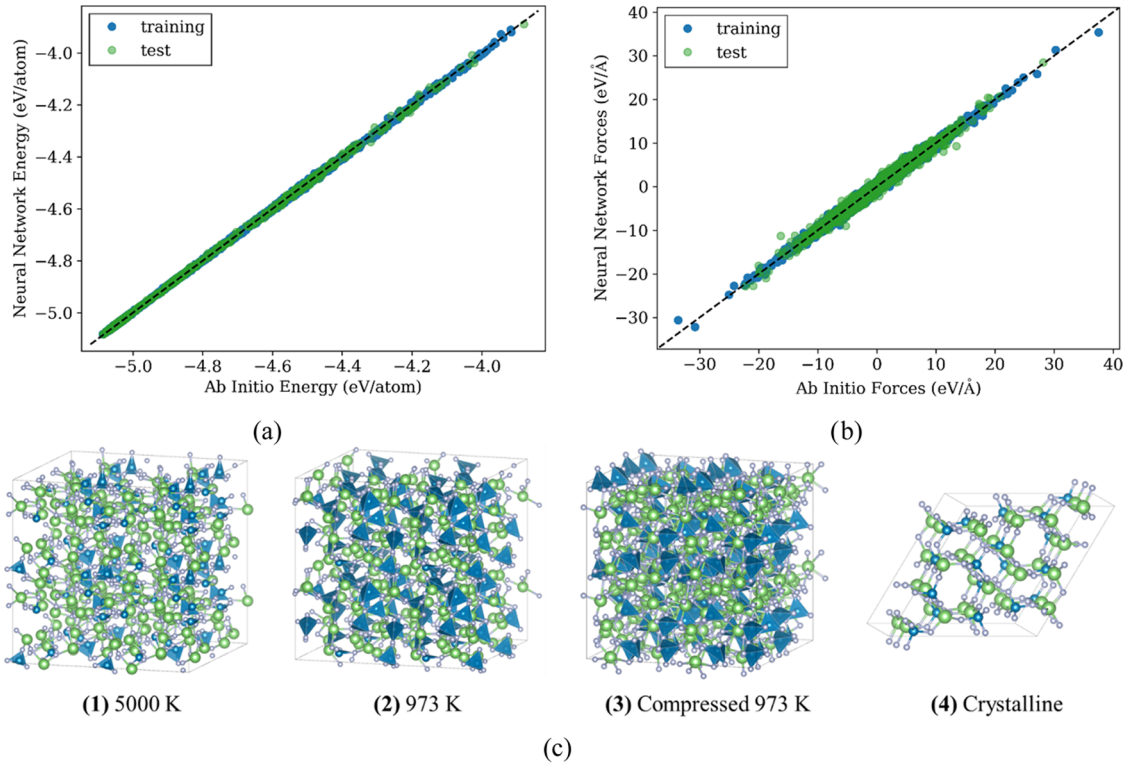


**Figure 5.** Graphical representations showing a 2 × 2 × 2 supercell for (a) NNIP vs AIMD prediction of potential energies, (b) NNP vs AIMD prediction of forces, and (c) structures of Flibe at (1) 5000 K, (2) 973 K, and (3) 973 K under a 15% isotropic compression used to train the NNIP. The unit cell for crystalline Flibe shown in (4) is used to test the trained network. Blue and green represent Be and Li, respectively.

**Table 3. Neural Network Potential Energy and Force Mean Average Error (MAE) for Training and Test Data Sets**

| | train (80%) | test (10%) |
|---|---|---|
| energy (meV/atom) [kJ/mol (Flibe)] | 1.75 [0.39] | 2.10 [0.47] |
| forces (eV/Å) | 0.081 | 0.084 |

by the neural network during training, this suggests that the Flibe NNIP is reasonably well fit and able to extrapolate to different structures and chemical environments. Moreover, the prediction accuracy for solid structures can always be increased by introducing more examples in the training set if needed.

The ability of the neural network potential to extrapolate over a longer time scale is also tested. An MD simulation was performed in LAMMPS using the NNIP.[16] First, energy minimization was performed on the atomic configuration. Then, the system was heated and equilibrated from 100 to 973 K over 15 ps. Finally, NVT simulation was performed at 973 K for 130 ps using a time step of 1 fs, which exceeds the time scale of simulations performed to generate the training data. Then, snapshots along the NNIP-MD trajectory were uniformly sampled to perform static DFT calculations. The calculated energies from DFT were compared to those calculated by the NNIP, as shown in Figure 6. Compared to DFT, the neural network predictions for energy were very accurate with less than 2 meV/atom error. Forces were also accurately calculated with an error of less than 0.08 eV/Å. These results are consistent with the errors found during training and testing. This shows that the NNIP is capable of interpolating the ab initio potential energy surface, thus extending accurate structure sampling over a longer time scale (far beyond the time scales involved in AIMD when generating training data). This greatly increases the confidence that the

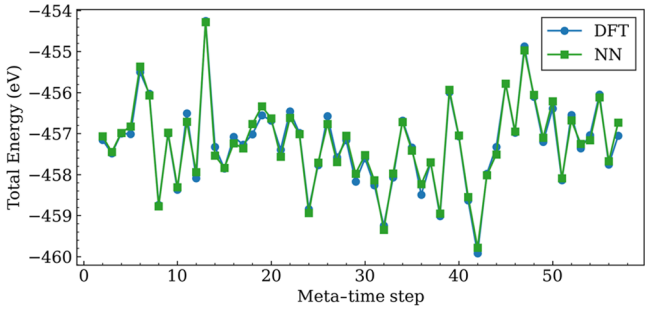


**Figure 6.** Neural network trajectory with each meta-time step representing 2 ps. Configurations are recalculated in DFT, and the ab initio energies are compared.

neural network can be used in large length scales and long-time-scale molecular dynamics simulations that are used for property prediction.

*3.2.2. Local Structure of Flibe.* To test the ability of the neural network potential to calculate disordered liquid structures in molten salts, the radial distribution function (RDF) and angular distributions computed from NN-based MD were compared to those from AIMD calculation. The AIMD simulation consisted of a system with 91 atoms (26 Li, 52 F, 13 Be) at 973 K and was run over 40 ps. For NNIP-MD simulations, the simulation cell was replicated in a 3 × 3 × 3 arrangement, which resulted in a much larger simulation cell of 2457 atoms. This yielded better statistics in the RDF calculation and allowed for examination of accuracy at larger length scales that are inaccessible by AIMD. The system was thermally equilibrated at 973 K over 15 ps before data was collected. Then, canonical ensemble simulations with the


https://doi.org/10.1021/acsami.1c00604
ACS Appl. Mater. Interfaces 2021, 13, 24582−24592

neural network potential were performed at 973 K for 50 ps. NVT simulations were performed at different cell volumes to fit to the Birch−Murnaghan equation of state as shown in Figure 7, from which density and bulk modulus were

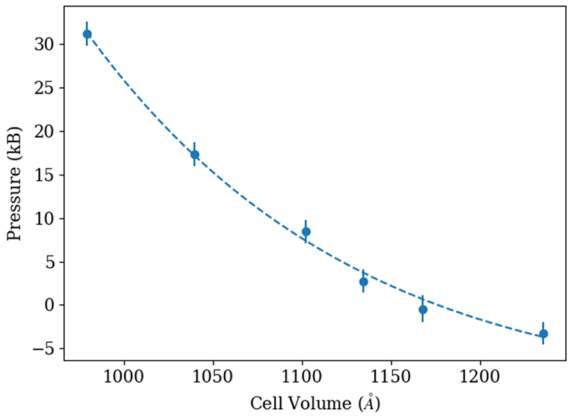


**Figure 7.** NNIP predicted equation of state for Flibe at 973 K. Calculated data (points) are fitted to the Birch−Murnaghan equation of state (dashed line).

obtained.[40,41] The equilibrium density was found to be 1815 kg/m$^3$, which is a 6% underprediction compared to the experimental value.[15] This error is most likely due to the lack of dispersion effects included in the DFT data that was used to train the NN model and the relatively low bulk modulus for Flibe, which was calculated to be ∼9.0 GPa. This is consistent with previous ab initio calculations for Flibe.[42] In comparison, our previous studies estimated that the average density of binary chlorides and fluorides is overestimated by 4% when using Grimme's D3 method,[43] and Nam found that Flibe density was overpredicted by ∼2% using Grimme's D2 method.[42,44] Dispersion can have effects on the calculated properties of molten salts but are generally not observed in fixed volume simulations.[45] However, it can influence the calculated equilibrium volume and melting transition, and as such, dispersion corrections should be appropriately parameterized and tested. This can be added to provide systematic improvement in neural network potential predictions.

The local structure predicted by NNIP, DFT, and polarizable ion model is compared in Figure 8. For PIM calculations, simulations were performed in CP2K[46] using parameters from a previous study.[47] Simulations were performed for 100 ps, with the first 10 ps used for equilibration.

For the RDFs in Figure 8a, NN (circles), DFT values (solid lines), and PIM (dashed lines) values show good agreement for all species pairs (Be−F, F−Li, F−F). NN-based RDFs follow the curvature of the DFT and PIM-based RDFs closely over the range from 0 to 6 Å, precisely matching the location and magnitude of the minima and maxima and the peak widths and heights. This indicates that the DFT and previously validated PIM[47] coordination distances and the coordination numbers between atomic species are well reproduced by the NNIP. Furthermore, the calculated first peak distances for Be−F, Li−F, and F−F are 1.5, 1.8, and 2.5 Å, which are close to their experimental values of 1.58, 1.85, and 2.56 Å, respectively.[48] In addition, the calculated fluorine coordination numbers (integral of the first peak in the RDF) of Li and Be are 4.0 and 4.0, compared to experimental values of 4.0 and 3.7, respectively. This indicates that DFT and consequently NNIP can accurately capture the local environment of ions in Flibe.

To calculate the angular distribution, the angle formed by triplets was tallied based on specified bond cutoff distances, and the distributions were normalized ($\int_0^{2\pi} f(\theta)\mathrm{d}\theta = 1$) to give $f(\theta_{ijk})$, where $i$, $j$, and $k$ represent the atomic species of each atom in the triplet. The cutoff distances were specified using the first minimum of each RDF, which are 2.7 Å for Li−F and 2.3 Å for Be−F. The angular distributions are found in Figure 8b, where the two prominent peaks are observed for F−Be−F and Be−F−Be. The peak value of F−Be−F is located at 108°, which represents a $BeF_2$ tetrahedral configuration, and the Be−F−Be represents corner-sharing tetrahedra with a median angle of 127°. These observations agree with our previous study,[13] where the detailed analysis was performed on the local and extended structures in Flibe, and Be−$F_4$ tetrahedral chains were observed with up to 4 Be atom centers. As shown in Figure 8b, the three-body interactions are accurately modeled by the NN (dashed lines), with the angular distributions almost exactly overlapping the AIMD (solid lines) results in

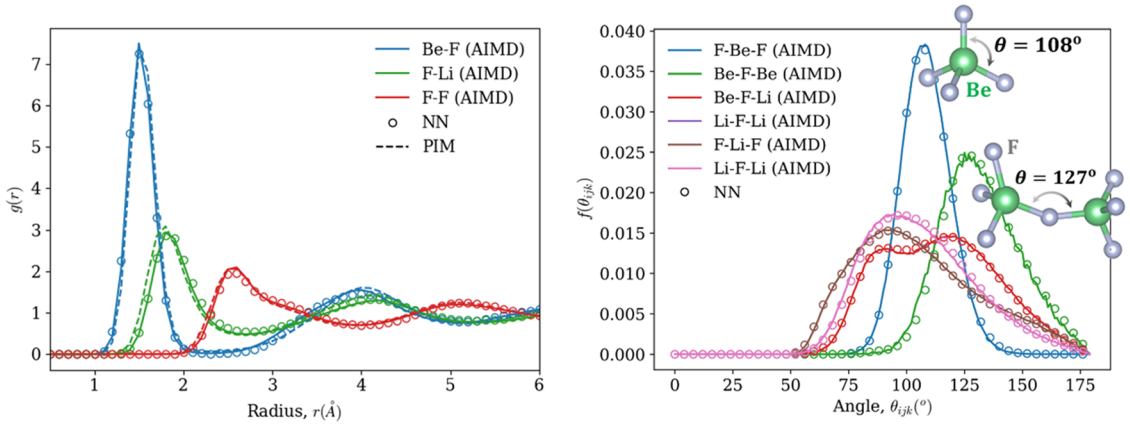


**Figure 8.** (a) Neural network potential, polarizable ion model, and DFT radial distribution functions obtained for Be−F, Li−F, and F−F pairs in Flibe. (b) Angular distribution functions of Flibe.



https://doi.org/10.1021/acsami.1c00604
ACS Appl. Mater. Interfaces 2021, 13, 24582−24592

Table 4. Neural Network Potential versus AIMD-Calculated Self-Diffusivity of Ions in Flibe at 973 K

| species | $D_{NN} \times 10^5$ (cm$^2$/s) | $D_{AIMD} \times 10^5$ (cm$^2$/s) | $D_{PIM} \times 10^5$ (cm$^2$/s) | $D_{EXP} \times 10^5$ (cm$^2$/s) |
|---|---|---|---|---|
| Be | 0.87 ± 0.13 | 0.83 ± 0.10 | 0.79 ± 0.08 | |
| F | 1.93 ± 0.19 | 1.73 ± 0.17 | 1.05 ± 0.15 | |
| Li | 5.12 ± 0.50 | 5.67 ± 0.52 | 3.72 ± 0.29 | 16.7 ± 10.0 |

every species combination. While bond angles in LiF-$BeF_2$ are also captured by current polarizable ion models,[49] the design and development of new model functional forms for more complex materials may require significant time and domain knowledge to determine the relevant effects.[34] This is particularly difficult in cases where there are many possible species, and interactions are not yet well understood. In contrast, NN architectures provide arbitrarily rich parameter spaces, which should scale well to chemically complex systems.

Overall, these results show that the NNIP can accurately predict local structures and chemistry that are calculated by electronic structural methods like DFT, further demonstrating the robustness of the NNIP. Since a much smaller simulation cell was used to train the neural network, these tests show that the potential extrapolates well to larger systems where many more local configurations are sampled. Furthermore, due to long-range Coulomb effects and the medium-range cutoff distance of NNIP (up to 7 Å), neural networks alone might not be expected to achieve high accuracy in ionic systems. Therefore, other studies have proposed explicit treatment on charge information together with the neural network prediction.[50] Yet, this was not found to be necessary for molten salts as shown in this work and previous work on NaCl molten salt.[51] The authors believe that this is likely due to the charge screening from local ionic solvation shells that limit long-range interactions.

*3.2.3. Ionic Diffusion.* Modeling atomic transport behavior is of practical relevance in molten salt applications, as it enables the prediction of important properties like viscosity, heat conduction, and species diffusion. Previous efforts have found that AIMD can accurately predict ionic self-diffusivity for a variety of binary and ternary fluoride salts.[13] This provides motivation for using a neural network potential to model the more expensive ab initio PES to calculate diffusivity and perform molecular dynamics for understanding transport behavior. The self-diffusivity is calculated using the block-averaging method, from the slope of the mean-squared displacement (MSD) as a function of time.[52] Here, the Einstein relationship is used

$$D = \frac{1}{6}\lim_{t\to\infty}\frac{\mathrm{d}}{\mathrm{d}t}(\mathrm{MSD}) = \frac{1}{6}\lim_{t\to\infty}\frac{\mathrm{d}}{\mathrm{d}t}\left(\frac{1}{N}\frac{1}{n_t}\sum_{n_t}^{j=1}\sum_{N}^{i=1}(r_i(t_j+\mathrm{d}t) - r_i(t_j))^2\right) \quad (7)$$

where MSD is determined for and averaged over subsets $n_t$ of the total trajectory and over all of the atoms $N$ of the same elemental type, $r_i(t)$ are the coordinates of atomic $i$ at time $t$, and d$t$ is the length of time spanned by each subset in time. For this calculation, a 91-atom simulation was used to allow for direct comparison between DFT and NN. The system is equilibrated at 973 K for 10 ps, and the simulation is performed over 70 ps using both NN potentials and AIMD. In addition, diffusivity calculated using the PIM potential is shown along with limited experimental results. These diffusivities for the species in Flibe are shown in Table 4, where the uncertainty values represent the 95% confidence intervals of the predictions.

In all cases (Be, F, and Li), the relative magnitudes of ionic diffusivities in AIMD are reproduced by both NNIP and PIM potentials and agree qualitatively with expectations based on the known structure and dynamics of Flibe.[8,47] Beryllium diffusivity is lowest at 0.79−0.87 × $10^{-5}$ cm$^2$/s due to the presence of $BeF_4$ tetrahedral polymer-like chains shown in Figures 5c and 8b. In contrast, the LiF in Flibe (66.6%LiF−33.3%$BeF_2$) is found to dissociate, producing free fluorine and lithium ions. As a result, the fluorine diffusivity is higher (some fluorine still bound to Be). For fluorine, NNIP results agreed with DFT within statistical uncertainty, while PIM diffusivity was 0.7 × $10^{-5}$ cm$^2$/s lower than DFT. For fluorine, one experimental result exists[53] but is believed to be unreliable based on our previous analysis and is therefore not used for comparison here.[13] The lithium diffusivity is the highest with DFT and NN values being around 5.12−5.67 × $10^{-5}$ cm$^2$/s. The lithium diffusivity values were again slightly lower for PIM, in which the calculated value was 3.72 ± 0.29 cm$^2$/s. For lithium, only one experimental study is available for comparison. The experimental Li measurement is closer to the DFT and NNIP calculations, but the experimental uncertainty is very large compared to the difference between values calculated by the different computational methods. Overall, the agreement between methods is good, as small differences are expected since the models are developed on different data. Further, the neural network prediction agrees with DFT within the uncertainty (±10−15%) for all cases, which is within the uncertainty of typical experiments. This provides a good indication that NNIP dynamics are accurate and bound only by the accuracy of the ab initio functionals used to train the model. Given reliable DFT functionals, NNIPs should be reasonably capable of calculating more demanding dynamics and transport properties such as viscosity or heat transfer coefficient.

*3.2.4. Computational Performance of Neural Network Potential.* The computational demand of the neural network potential for Flibe is examined in this section. Scaling tests were performed, and simulation times are compared between DFT, neural network potentials, and polarizable ion models. Simulations for these tests were performed on the Engaging cluster in the Massachusetts Green High Performance Computing Center (MGHPCC) facility and the Frontera Cluster in the Texas Advanced Computing Center (TACC). The Engaging cluster consists of nodes with 2 × 16 Intel Xeon 2.1 GHz cores, connected with an Infiniband interconnect with a bandwidth of 4 × 14 Gb/s node-to-node transfer and 0.7 ms of latency. On Frontera, nodes consisted of 28 × 2 Intel Xeon Platinum 8280 2.7 GHz processors connected via a HDR-100 Mellanox InfiniBand. Parallelization in DFT is performed using VASP recommendations based on machine architecture, with 32 cores (one node) operating on each orbital.[18] MDs with neural network potentials are performed in a parallel


https://doi.org/10.1021/acsami.1c00604
ACS Appl. Mater. Interfaces 2021, 13, 24582−24592

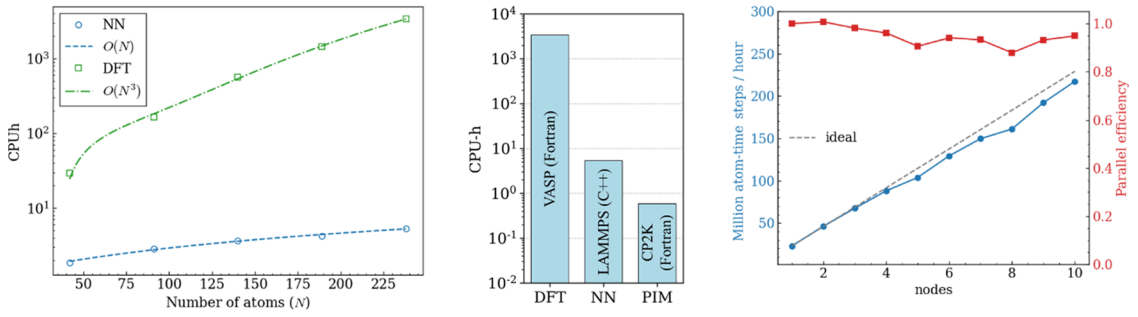


**Figure 9.** (a) CPU-hours for 1000 MD time steps versus number of atoms, (b) CPU-hour comparison between DFT, NN, and PIM models for 1000 MD time steps of a 238-atom system, (c) computational speedup for the Flibe system with 91 000 atoms. Each node represents 56 cores on the TACC Frontera system. The black dashed line represents ideal efficiency.

installation of LAMMPS.[54] An MD simulation using PIM was performed using a parallel installation of CP2K.[46]

The computational demand of neural networks is compared to those of PIM and DFT, as shown in Figure 9. The required core-hours to run 1000 time steps of molecular dynamics simulation is shown for Flibe systems of different sizes. As expected, DFT scales roughly as $\sim O(N^3)$, where $N$ is the number of atoms. In contrast, the neural network potentials scale like classical potentials, roughly as $\sim O(N)$. Thus, the computational gain from using a neural network potential grows with increasing system sizes. With a system with 238 atoms in 14.2 × 14.2 × 14.2 Å$^3$, periodic cell effects are very small and a variety of calculated thermokinetic properties are generally expected to be well converged.[42] For a system of this size, the required calculation time is 3379.0 CPU-hours for 1000 DFT time steps. In comparison, the same calculations can be done using the neural network potential with 5.3 CPU-hours, which is 630 times faster. The PIM model performs the same calculation in 0.6 CPU-hours, which is 9 times faster than the NN, as shown in Figure 9b. While a neural network requires more time than classical methods, various network optimization techniques can be employed to reduce the difference.[55] Further, NNs have the potential to excel in areas that could be challenging for classical models, such as for systems with many simultaneous components, chemical reactions, or hydrogen speciation.[13,56,57] Here, linear scaling with $N$ provides significant capability for chemical and size and extensibility in computation.

In addition to scaling performance with respect to $N$ (atoms), a strong scaling test across multiple processors was also tested by performing MD simulations using 56−560 cores. The results are shown in Figure 9c. The system simulated is Flibe at 973 K with 91 000 atoms. At each time step, the evaluation of energies and forces requires relatively simple matrix multiplication and algebraic operations required by the calculation of forward pass of the neural network. This is performed via a LAMMPS interface plugin provided by PANNA, which is written in C++.[24] Thus, the parallelization shown in Figure 9c benefits from LAMMPS optimization, which provides robust spatial decomposition algorithms using message passing interface (MPI) parallelization.[54,58] As shown, scaling is near-ideal (>98%) if more than 30 000 atoms are used per node. The efficiency drops slightly if more nodes are used. At 9100 atoms per node (10 nodes), the efficiency is 94%. This demonstrates that the calculations generally scale well with the number of processors used for a large simulation. Further, additional speed improvements in the future can be gained by pruning the network to reduce the total number of floating-point operations per energy calculation or by looking at different parallelization strategies. This includes optimizing a hybrid MPI (distributed memory) and OpenMP (shared memory) parallelization scheme for calculations using many processors or utilizing graphics-based acceleration methods for significantly larger systems.[59]

From experience, the calculation of salt properties such as equation of state or diffusion activation energy can require tens-to-hundreds of thousands of DFT calculations.[13] In such cases, the use of robust and flexible NNIP molecular dynamics provides more than 3 orders of magnitude computational time reduction over AIMD, reducing the time to determine a single thermophysical property from several weeks to hours. Therefore, the NNIP could greatly increase the efficiency of high-throughput calculation of molten salt properties. Further, larger systems with more interesting properties like radiation damage or defect chemistry can potentially be studied.

## 4. CONCLUSIONS

Robust and versatile NNIPs have been developed for the common salt constituent LiF and a prototype salt Flibe (66% LiF−33%BeF2). We showed that a diverse set of local atomic environments could be captured using radial and angular symmetry functions based on the sum of Gaussian functions and used as inputs to train versatile interatomic potentials. For LiF, we showed that an NNIP can simultaneously capture dimer interactions (F−F, Li−Li, Li−F), deformed solids at 0 K, solids near the melting point, through the melting transition, and toward high-temperature liquids with DFT-level accuracies of <2 meV/atom. Further, the LiF NNIP can accurately predict energies of surfaces that were not used for training, suggesting that neural networks could properly extrapolate to configurations differing from experience. Such a behavior is highly desirable in NNIPs, where the physical interactions are not explicitly encoded, and the model parameters are difficult to interpret. The Flibe NNIP trained is able to simulate molten salt at 973 K (operating temperature of most reactor systems), compressed Flibe up to 15%, and high-temperature salt exceeding 5000 K. By introducing structures under extreme conditions, configurational sampling was greatly improved. The Flibe NNIP has been integrated into the LAMMPS[29] molecular dynamics engine using the PANNA package[24] and shows highly consistent accuracy for both extended time scale and length-scale simulations. Particularly, the NNIP structural


https://doi.org/10.1021/acsami.1c00604
ACS Appl. Mater. Interfaces 2021, 13, 24582−24592

(local coordination environment) and transport property prediction of Flibe are consistent with DFT and previous experimental results.

In this work, NNIPs have been shown to be highly adaptable to a variety of local environments while maintaining near ab initio accuracy. This feature is very desirable for applications to real systems, which involve many components and span wide thermodynamic conditions. This demonstrates a significant advantage over classical interatomic potentials that are typically fit for a specific application and have limitations of accuracy and generality, particularly in reactive systems and systems of growing complexity. Due to its ability to approximate an arbitrarily complex functional form, neural networks enable robust modeling of interatomic interactions of increasingly complex systems. Moreover, these potentials are able to accelerate property computations by more than 3 orders of magnitude and far beyond the accessible time and length scales of ab initio methods while showing strong scaling efficiency with a large number of processors. As such, neural networks are demonstrated to provide a promising direction for multicomponent ionic liquid systems such as molten salts that would be difficult to study using either ab initio or classical methods alone. In future work, these potentials will be applied to study more computationally challenging systems, which could enable dramatically accelerated screening and allow unprecedented interpolation across compositional and real operating space.

## AUTHOR INFORMATION


### Corresponding Author

**Stephen T. Lam** − *Department of Chemical Engineering, University of Massachusetts Lowell, Lowell, Massachusetts 01854, United States; Department of Nuclear Science and Engineering, Massachusetts Institute of Technology, Cambridge, Massachusetts 02139, United States;* orcid.org/0000-0002-7683-1201; Email: stephen_lam@uml.edu

### Authors

**Qing-Jie Li** − *Department of Nuclear Science and Engineering, Massachusetts Institute of Technology, Cambridge, Massachusetts 02139, United States*

**Ronald Ballinger** − *Department of Nuclear Science and Engineering, Massachusetts Institute of Technology, Cambridge, Massachusetts 02139, United States; Department of Materials Science and Engineering, Massachusetts Institute of Technology, Cambridge, Massachusetts 02139, United States*

**Charles Forsberg** − *Department of Nuclear Science and Engineering, Massachusetts Institute of Technology, Cambridge, Massachusetts 02139, United States*

**Ju Li** − *Department of Nuclear Science and Engineering, Massachusetts Institute of Technology, Cambridge, Massachusetts 02139, United States; Department of Materials Science and Engineering, Massachusetts Institute of Technology, Cambridge, Massachusetts 02139, United States;* orcid.org/0000-0002-7841-8058

Complete contact information is available at: https://pubs.acs.org/10.1021/acsami.1c00604


### Notes

The authors declare no competing financial interest.

## ACKNOWLEDGMENTS

S.L. acknowledges funding support from the National Science and Engineering Research Council of Canada and the Shanghai Institute of Applied Physics. Q.-J.L. and J.L. acknowledge support by the Department of Energy, Office of Nuclear Energy, Nuclear Energy University Program (NEUP) under Award Number DE-NE0008751. The authors would like to acknowledge Thomas Beck and Yu Shi from the University of Cincinnati for assisting with the CP2K calculation and Emine Kucukbenli from Boston University for addressing technical inquiries related to PANNA.

## REFERENCES


(1) Wang, Y.; Vogel, A.; Sachs, M.; Sprick, R. S.; Wilbraham, L.; Moniz, S. J. A.; Godin, R.; Zwijnenburg, M. A.; Durrant, J. R.; Cooper, A. I.; Tang, J. Current Understanding and Challenges of Solar-Driven Hydrogen Generation Using Polymeric Photocatalysts. *Nat. Energy* **2019**, *4*, 746−760.

(2) Frangini, S.; Masi, A. Molten Carbonates for Advanced and Sustainable Energy Applications: Part II. Review of Recent Literature. *Int. J. Hydrogen Energy* **2016**, *41*, 18971−18994.

(3) Voisin, T.; Erriguible, A.; Aymonier, C. A New Solvent System: Hydrothermal Molten Salt. *Sci. Adv.* **2020**, *6*, No. eaaz7770.

(4) Bell, S.; Steinberg, T.; Will, G. Corrosion Mechanisms in Molten Salt Thermal Energy Storage for Concentrating Solar Power. *Renewable Sustainable Energy Rev.* **2019**, *114*, No. 109328.

(5) Delpech, S.; Cabet, C.; Slim, C.; Picard, G. S. Molten Fluorides for Nuclear Applications. *Mater. Today* **2010**, *13*, 34−41.

(6) Rollet, A. L.; Salanne, M. Studies of the Local Structures of Molten Metal Halides. *Annu. Rep. Prog. Chem., Sect. C: Phys. Chem.* **2011**, *107*, 88−123.

(7) Williams, D. F.; Toth, L. M.; Clarno, K. T. T. *Assessment of Candidate Molten Salt Coolants for the Advanced High-Temperature Reactor (AHTR)*, ORNL/TM-2006/69; Oak Ridge National Laboratory: Oak Ridge, Tennessee, 2006.

(8) Heaton, R. J.; Brookes, R.; Madden, P. A.; Salanne, M.; Simon, C.; Turq, P. A First-Principles Description of Liquid BeF2 and Its Mixtures with LiF: 1. Potential Development and Pure BeF2. *J. Phys. Chem. B* **2006**, *110*, 11454−11460.

(9) Salanne, M.; Rotenberg, B.; Jahn, S.; Vuilleumier, R.; Simon, C.; Madden, P. A. Including Many-Body Effects in Models for Ionic Liquids. *Theor. Chem. Acc.* **2012**, *131*, No. 1143.

(10) Smith, A. L.; Capelli, E.; Konings, R. J. M.; Gheribi, A. E. A New Approach for Coupled Modelling of the Structural and Thermo-Physical Properties of Molten Salts. Case of a Polymeric Liquid LiF-BeF2. *J. Mol. Liq.* **2020**, *299*, No. 112165.

(11) Bedrov, D.; Piquemal, J.; Borodin, O.; Mackerell, A. D.; Roux, B.; Schröder, C. Molecular Dynamics Simulations of Ionic Liquids and Electrolytes Using Polarizable Force Fields. *Chem. Rev.* **2019**, *119*, 7940−7995.

(12) Defever, R. S.; Wang, H.; Zhang, Y.; Maginn, E. J. Melting Points of Alkali Chlorides Evaluated for a Polarizable and Non-Polarizable Model. *J. Chem. Phys.* **2020**, *153*, No. 011101.

(13) Lam, S. T.; Li, Q.-J.; Mailoa, J. P.; Forsberg, C.; Ballinger, R.; Li, J. The Impact of Hydrogen Valence on Its Bonding and Transport in Molten Fluoride Salts. *J. Mater. Chem. A* **2021**, *9*, 1784−1794.

(14) Janz, G. J.; Gardner, G. L.; Krebs, U.; Tomkins, R. P. T. Molten Salts: Volume 4, Part 1, Fluorides and Mixtures Electrical Conductance, Density, Viscosity, and Surface Tension Data. *J. Phys. Chem. Ref. Data* **1974**, *3*, 1−115.

(15) Janz, G. Thermodynamic and Transport Properties for Molten Salts Correlation Equations for Critically Evaluated Density. *J. Phys. Chem. Ref. Data* **1988**, *17*, 1−309.

(16) Kohn, W.; Sham, L. J. Self-Consistent Equations Including Exchange and Correlation Effects. *Phys. Rev.* **1965**, *140*, A1133−A1138.

(17) Kühne, T. D. Second Generation Car-Parrinello Molecular Dynamics. *Wiley Interdiscip. Rev. Comput. Mol. Sci.* **2014**, *4*, 391−406.
(18) Kresse, G.; Furthmüller, J. Efficient Iterative Schemes for Ab Initio Total-Energy Calculations Using a Plane-Wave Basis Set. *Phys. Rev. B* **1996**, *54*, 11169−11186.
(19) Hellström, M.; Behler, J. Neural Network Potentials in Materials Modeling BT. In *Handbook of Materials Modeling: Methods: Theory and Modeling*; Andreoni, W.; Yip, S., Eds.; Springer International Publishing: Cham, 2020; pp 661−680.
(20) Botu, V.; Batra, R.; Chapman, J.; Ramprasad, R. Machine Learning Force Fields: Construction, Validation, and Outlook. *J. Phys. Chem. C* **2017**, *121*, 511−522.
(21) Behler, J.; Parrinello, M. Generalized Neural-Network Representation of High-Dimensional Potential-Energy Surfaces. *Phys. Rev. Lett.* **2007**, *98*, No. 146401.
(22) Ko, T. W.; Finkler, J. A.; Goedecker, S.; Behler, J. A Fourth-Generation High-Dimensional Neural Network Potential with Accurate Electrostatics Including Non-Local Charge Transfer. *Nat. Commun.* **2021**, *12*, No. 398.
(23) Wang, H.; Zhang, L.; Han, J.; Weinan, E. DeePMD-Kit: A Deep Learning Package for Many-Body Potential Energy Representation and Molecular Dynamics. *Comput. Phys. Commun.* **2018**, *228*, 178−184.
(24) Lot, R.; Pellegrini, F.; Shaidu, Y.; Küçükbenli, E. PANNA: Properties from Artificial Neural Network Architectures. *Comput. Phys. Commun.* **2020**, *256*, No. 107402.
(25) Artrith, N.; Morawietz, T.; Behler, J. High-Dimensional Neural-Network Potentials for Multicomponent Systems: Applications to Zinc Oxide. *Phys. Rev. B* **2011**, *83*, No. 153101.
(26) Smith, J. S.; Isayev, O.; Roitberg, A. E. ANI-1: An Extensible Neural Network Potential with DFT Accuracy at Force Field Computational Cost. *Chem. Sci.* **2017**, *8*, 3192−3203.
(27) Li, Q.; Ku, E.; Lam, S.; Khaykovich, B.; Li, Q.; Ku, E. Development of Robust Neural-Network Interatomic Potential for Molten Salt. *Cell Press Phys. Sci.* **2021**, *2*, No. 100359.
(28) Kingma, D. P.; Ba, J. In *Adam: A Method for Stochastic Optimization*, 3rd International Conference on Learning Representations (ICLR): San Diego, CA, USA, 2015; pp 1−15.
(29) Plimpton, S. Fast Parallel Algorithms for Short-Range Molecular Dynamics. *J. Comput. Phys.* **1995**, *117*, 1−19.
(30) Jain, A.; Dixit, R. C. In *B 1 to B 2 Structural Phase Transition in LiF Under Pressure*, AIP Conference Proceedings; AIP Publishing LLC, 2018; Vol. *1953*, p 040013.
(31) Finch, G. J.; Fordham, S. The Effect of Crystal-Size on Lattice-Dimensions. *Proc. Phys. Soc.* **1936**, *48*, 85−94.
(32) Rubbo, M.; Bruno, M.; Prencipe, M. Thermodynamic Study of Reconstructed Crystal Surfaces.: The Octopolar (111) Face of LiF Crystals. *Surf. Sci.* **2015**, *632*, 180−184.
(33) Van Der Hoff, B. M. E.; Benson, G. C. A Quantum-Mechanical Calculation of the Surface Energy of Crystalline Lithium Fluoride. *J. Chem. Phys.* **1954**, *22*, 475−480.
(34) Salanne, M.; Simon, C.; Turq, P.; Ohtori, N.; Madden, P. A. A. Modeling of Molten Salts. In *Molten Salts Chemistry*; Elsevier Inc., 2013; pp 1−16.
(35) Collins, D. M.; Mahar, M. C.; Whitehurst, F. W. Bonding in Lithium Tetrafluoroberyllate(II). *Acta Crystallogr., Sect. B: Struct. Sci.* **1983**, *39*, 303−306.
(36) Seiler, P. Estimation of Ionicity Coefficients in Li2 Be F4 Crystals by X-Ray Diffraction. *Acta Crystallogr., Sect. B: Struct. Sci.* **1993**, *49*, 223−235.
(37) Lejaeghere, K.; Van Speybroeck, V.; Van Oost, G.; Cottenier, S. Error Estimates for Solid-State Density-Functional Theory Predictions: An Overview by Means of the Ground-State Elemental Crystals. *Crit. Rev. Solid State Mater. Sci.* **2014**, *39*, 1−24.
(38) Overhauser, A. W. Crystal Structure of Lithium at 4.2 K. *Phys. Rev. Lett.* **1984**, *53*, 64−65.
(39) Larsen, F. K.; Hansen, N. K. Diffraction Study of the Electron Density Distribution in Beryllium Metal. *Acta Crystallogr., Sect. B: Struct. Sci.* **1984**, *40*, 169−179.
(40) Birch, F. Finite Elastic Strain of Cubic Crystals. *Phys. Rev.* **1947**, *71*, 809−824.
(41) Murnaghan, F. D. The Compressibility of Media under Extreme Pressures. *Proc. Natl. Acad. Sci. U.S.A.* **1944**, *30*, 244−247.
(42) Nam, H. O.; Bengtson, A.; Vörtler, K.; Saha, S.; Sakidja, R.; Morgan, D. First-Principles Molecular Dynamics Modeling of the Molten Fluoride Salt with Cr Solute. *J. Nucl. Mater.* **2014**, *449*, 148−157.
(43) Lam, S. T. Accelerated Atomistic Prediction of Structure, Dynamics and Material Properties in Molten Salts. Ph.D. Thesis, Massachusetts Institute of Technology: Cambridge, MA, 2020.
(44) Grimme, S.; Antony, J.; Ehrlich, S.; Krieg, H. A Consistent and Accurate Ab Initio Parametrization of Density Functional Dispersion Correction (DFT-D) for the 94 Elements H-Pu. *J. Chem. Phys.* **2010**, *132*, No. 154104.
(45) Corradini, D.; Marrocchelli, D.; Madden, P. A.; Salanne, M. The Effect of Dispersion Interactions on the Properties of LiF in Condensed Phases. *J. Phys. Condens. Matter* **2014**, *26*, No. 244103.
(46) Kühne, T. D.; Iannuzzi, M.; Del Ben, M.; Rybkin, V. V.; Seewald, P.; Stein, F.; Laino, T.; Khaliullin, R. Z.; Schütt, O.; Schiffmann, F.; Golze, D.; Wilhelm, J.; Chulkov, S.; Bani-Hashemian, M. H.; Weber, V.; Borštnik, U.; Taillefumier, M.; Jakobovits, A. S.; Lazzaro, A.; Pabst, H.; Müller, T.; Schade, R.; Guidon, M.; Andermatt, S.; Holmberg, N.; Schenter, G. K.; Hehn, A.; Bussy, A.; Belleflamme, F.; Tabacchi, G.; Glöß, A.; Lass, M.; Bethune, I.; Mundy, C. J.; Plessl, C.; Watkins, M.; VandeVondele, J.; Krack, M.; Hutter, J. CP2K: An Electronic Structure and Molecular Dynamics Software Package -Quickstep: Efficient and Accurate Electronic Structure Calculations. *J. Chem. Phys.* **2020**, *152*, No. 194103.
(47) Salanne, M.; Simon, C.; Turq, P.; Heaton, R. J.; Madden, P. A.; Brookes, R.; Madden, P. A.; Salanne, M.; Simon, C.; Turq, P.; Heaton, R. J.; Madden, P. A. A First-Principles Description of Liquid BeF2 and Its Mixtures with LiF: 2. Network Formation in LiF-BeF2. *J. Phys. Chem. B* **2006**, *110*, 11461−11467.
(48) Vaslow, F.; Narten, A. H. Diffraction Pattern and Structure of Molten BeF 2 −LiF Solutions. *J. Chem. Phys.* **1973**, *59*, 4949−4954.
(49) Salanne, M.; Madden, P. A. Polarization Effects in Ionic Solids and Melts. *Mol. Phys.* **2011**, *109*, 2299−2315.
(50) Morawietz, T.; Sharma, V.; Behler, J. A Neural Network Potential-Energy Surface for the Water Dimer Based on Environment-Dependent Atomic Energies and Charges. *J. Chem. Phys.* **2012**, *136*, No. 064103.
(51) Li, Q.; Kucukbenli, E.; Lam, S.; Khaykovich, B.; Kaxiras, E.; Li, J. A Neural Network Interatomic Potential for Molten NaCl. *Bull. Am. Phys. Soc.* **2020**, *65*, No. M45.00011.
(52) Rapaport, D. C.; Rapaport, D. C. R. *The Art of Molecular Dynamics Simulation*; Cambridge University Press, 2004.
(53) Janz, G. J.; Bansal, N. P. Molten Salts Data: Diffusion Coefficients in Single and Multi Component Salt Systems. *J. Phys. Chem. Ref. Data* **1982**, *11*, 505−693.
(54) Plimpton, S. Short-Range Molecular Dynamics. *J. Comput. Phys.* **1997**, *117*, 1−42.
(55) Han, S.; Pool, J.; Tran, J.; Dally, W. J. Learning Both Weights and Connections for Efficient Neural Network. In *Advances in Neural Information Processing Systems*; Cortes, C.; Lawrence, N.; Lee, D.; Sugiyama, M.; Garnett, R., Eds.; Curran Associates, Inc., 2015; Vol. *28*, pp 1135−1143.
(56) Behler, J. First Principles Neural Network Potentials for Reactive Simulations of Large Molecular and Condensed Systems. *Angew. Chem., Int. Ed.* **2017**, *56*, 12828−12840.
(57) Heuer, A. Comparing Induced Point-Dipoles and Drude Oscillators. *Phys. Chem. Chem. Phys.* **2015**, *17*, 14297−14306.
(58) Singraber, A.; Behler, J.; Dellago, C. Library-Based LAMMPS Implementation of High-Dimensional Neural Network Potentials. *J. Chem. Theory Comput.* **2019**, *15*, 1827−1840.
(59) Glaser, J.; Nguyen, T. D.; Anderson, J. A.; Lui, P.; Spiga, F.; Millan, J. A.; Morse, D. C.; Glotzer, S. C. Strong Scaling of General-Purpose Molecular Dynamics Simulations on GPUs. *Comput. Phys. Commun.* **2015**, *192*, 97−107.


https://doi.org/10.1021/acsami.1c00604
*ACS Appl. Mater. Interfaces* 2021, 13, 24582−24592